# Distortion Correction in 3D-Modeling of Roots for Plant Phenotyping

T. K. Das Nakini and G. N. DeSouza

Vision-Guided and Intelligent Robotics Lab
Electrical and Computer Department
University of Missouri

**Abstract.** Root Phenotyping is an important tool in predicting the life and growth of plants. Many systems have been developed to automate the process of extracting root traits using 3D imaging system, however, not many of those systems corrected for the distortions that frequently appear during this process. In this paper we present a new method to compensate for light refractions that occur in the gel-based platforms for growing plants. As our results demonstrate, our method provides an accurate 3D point cloud containing the coordinates of the surface of the root system with error smaller than 0.02mm in average and standard deviation of less than 0.3mm.

**Keywords:** root phenotyping, gel-based media, hydroponic substrate, glass cylinder, distortion correction, 3D modeling

## 1 Introduction

Root System Architecture (RSA) is the spatial representation of a plant root system [24]. It plays a vital role in determining the life and growth of plants and hence, it is becoming one of the main focus of Computer Vision (CV) researchers in the field of biology and plant sciences. Indeed, many researchers have long correlated root traits present in the various RSAs to physiological functions of the plant, such as resistance to drought [9, 30], carbon allocation [4], phosphorous and nitrogen affinity [5, 22, 42], nutrient-acquisition capacity, etc. However, due to the practical difficulties in measuring and classifying RSAs, root phenotyping had, at least until recently, received little attention from the CV community. Among these difficulties is the ability to measure root traits without destroying the plants. In that sense, some researchers opted to grow plants in translucent gel-based media [8]. This approach allowed for the inspection of the plant while still inside a cylinder using, for example, simple two-dimensional (2D) imaging. In fact, 2D imaging was not only the first, but it is still likely the most popular tool for studying RSAs [23, 29, 7]. Unfortunately, while rich in details and extensively exploited, 2D features are quite limited by the possibility of self occlusion in the RSA, the high density of some roots, perspective distortions, etc. For that reason, researchers started to shift their attention to three dimensional (3D) modeling of RSAs [18, 8, 36]. In that case, however, distortion becomes a major problem, since the refractive nature of light passing through gel-glass media makes it virtually impossible to register raw images obtained from different viewing angles – a required step in any method for 3D modeling.

In this paper, our main goal is exactly to handle distortions caused by the refraction of light during the creation of 3D models of roots. This same distortion problem has been addressed in [39]. However, in that work, the authors assumed the simple case of a spot laser range finder that could

move up and down perpendicular to the cylinder vertical axis. Later, in [38], the authors extended that idea to accommodate for a vertical laser stripe. At that time, however, the surface of the media was considered flat and the thickness of the glass was not taken into consideration. In contrast, the main contribution of this research is to provide the first holistic distortion model for 3D imaging of RSA using structure light scanners and a gel-based platform for growing soybean. In summary, here, it will be explained how to achieve a clear, undistorted 3D model as the one shown in Figures 1a-d, as opposed to the 3D models created from distorted data in Figures 1e-h.



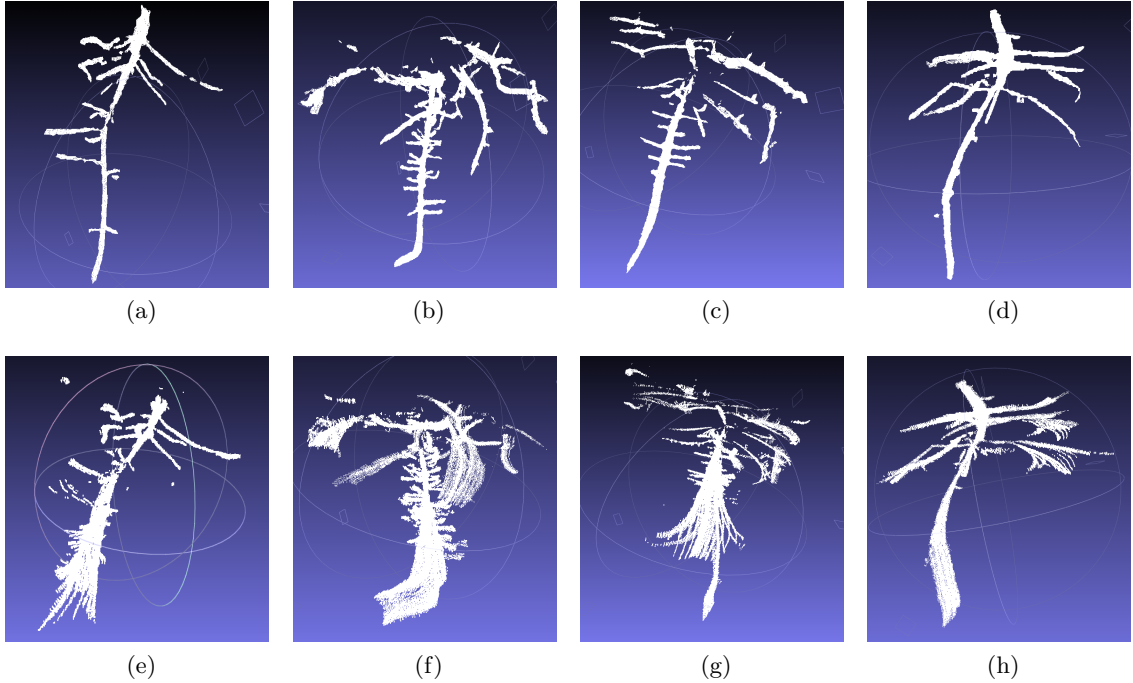|     |     |     |     |
| (a) | (b) | (c) | (d) |

| (e) | (f) | (g) | (h) |

Fig. 1: 3D Models of four different families of soybean: in (a) - (d) the undistorted models after the proposed corrections; and in (e) - (h) the raw, distorted models.

## 2   Background and Related Works

In the field of computer vision, imaging systems can be classified into two groups: 1) passive; and 2) active sensing. In passive sensing methods, the images are collected from different viewing angles using only the natural ambient lights [27, 12, 25, 21]. Later, those multiple images must be corresponded and *stitched* together to create a single 3D cloud of points. In active sensing, approaches can be divided into three groups depending on the type of sensor used: time-of-flight (ToF) sensors, structured-light scanners (SLS), and resonance sensors [6, 20].

In the first group, ToF, we will find sensors that measure the actual time it takes for the signal to bounce off the object (e.g. sound echoes), or those that instead resort to measuring phase changes

in the returned signal to infer the actual distance (e.g most of the sensors with light-spectrum or higher wavelengths). In either cases, ToF sensors are usually quite expensive, and therefore, they lost popularity in the computer vision circles to recent SLS. In this case, a SLS uses an external light or energy source to project fixed or moving patterns or "lighting structures" onto the scene. These patterns deform around the objects indicating their depths, or ranges from the sensor. Examples of SLS's include those using: 1) alternating illuminated-dark stripes; 2) dot patterns (usually in the near IR spectrum); and 3) a moving, thin laser stripe. Early works with SLS's date back to almost forty years ago [1, 16, 2, 41] but they are still popular in newer hardware versions such as the Microsoft Kinect. Finally, the resonance sensors employ strong energy sources – e.g. from X-ray emitters – that penetrate the object causing resonance on the chemical components or particles of the object lying on a plane created by another energy source – e.g. from a magnetic field. The magnetic field is controlled so that the plane is successively moved up or down, *slicing* the object into almost contiguous images.

As with the passive sensing, and despite the quite different principles employed by the active sensing systems, they also require the multiple range images or slices to be registered with one another while creating a single and complete 3D model.

In terms of root phenotyping, imaging systems can be broadly divided into two groups: destructive and non-destructive. In destructive approaches, the roots are quickly excavated, so they can be immediately imaged and analyzed [34]. By doing so, the roots are often damaged and the soils irreparably disturbed, making it impossible to image that same root under the same conditions in the future. On the other hand, in non-destructive methods, the roots are grown in translucent media, which allows for proper imaging systems to continuously create 2D or 3D models for future analysis. In such cases, the plant remains virtually undisturbed and temporal analyses of the root growth and responses to stress are possible.

Typical 3D modeling systems include: 1) structured-light scanners (e.g. laser) and multi-stereopsis based setups [26, 28, 10, 33, 8]; 2) Magnetic Resonance Imaging (MRI) or Nuclear Magnetic Resonance (NMR) [37, 31, 18, 36]; and 4) X-ray Computerized Axial Tomography (CAT) or simply Computerized Tomography (CT) [13, 14, 35].

Most of these systems, e.g. MRI, NMR and CT, are quite expensive and complex in nature. In the original CT technology, for example, the use of cone-shape beams caused the image of the object to become magnified. In order to compensate for this magnification, CT equipment started to use synchrotron emitters, which instead keep the beams almost parallel. In turn, these orthogonal projections cause artifacts in the image which must be eliminated together with other artifacts that also appear due to incomplete sampling of the so-called Radon space [19].

Another problem from which, in this case, all 3D imaging systems for gel-based platforms suffer is image distortion. This distortion is due to the refractive nature of light, or EM waves in general, that bends as it traverses different media. In order to cope with this problem, many researchers have opted to: 1) use optical correction tanks [33, 8]; 2) increase the size of the cylinder with respect to the volume of the RSA to minimize the effects of distortion [17, 32]; or 3) simply ignore the distortions [10, 40, 11].

In the case of correction tanks, even though they may indeed eliminate distortion errors, the final setup is quite cumbersome due to the extra tank that needs to be added to the system; the care with its positioning with respect to the root/gel cylinder; and the positioning of the principle axis of the camera perpendicular to the tank surface.

Similarly, the reliance on a small root systems in comparison to the volume of the gel cylinder as a method to minimize distortions is not always possible or easy to achieve. In the case of rice

and other cereal grains with small RSAs, this may not represent a problem. However, for soybean, corn and many other plants with larger root systems, making sure that the root is confined to the interior of the cylinder may represent a large waste of gel and the associated increase in the cost for root phenotyping per plant.

In contrast, here we propose a new method for correcting distortion in 3D modeling of root systems inside a gel-based platform. Our system is quite less expensive and comparatively much simpler than other active sensing systems. Also, and possibly more importantly, there are little constraints on the positioning of any of its components – camera, laser emitter, gel cylinder, etc. In fact, both the system's intrinsic and extrinsic parameters are automatically calibrated. That includes, of course, the distortion parameters used later on while imaging a root system. These distortion parameters originate from the many refractions of light from the emitter, through the glass-gel, and back onto the camera sensor. As our results demonstrate, at the end of the process, our systems provides a 3D point cloud of the surface of the root with error smaller than 0.02mm in average and a standard deviation of less than 0.3mm.
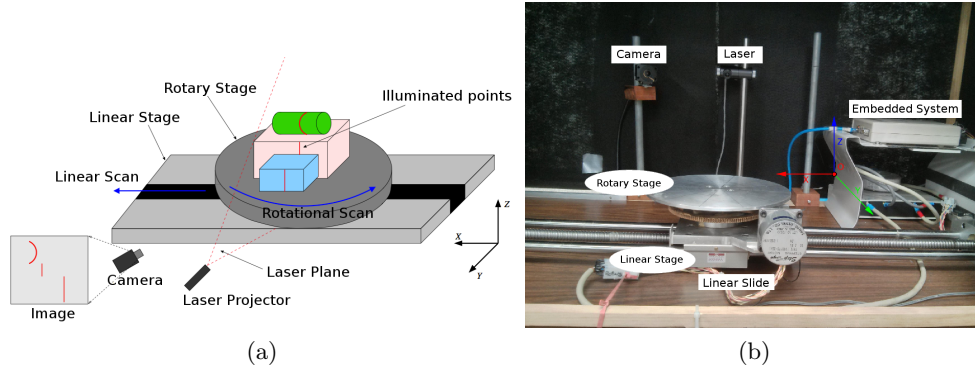


Fig. 2: Laser Stripe Structured-Light Scanner: a) Depiction of the principle behind a SLS using a laser stripe: the laser stripe conforms to the contour of the object in the scene, which provides to the camera a measurement of the object's depth and shape; b) Actual system used in this research. Indications of the position of the camera, the position of the laser, the coordinate frames, etc. are superimposed onto the picture.

## 3   Proposed Method

In this work, a structured-light system (SLS) using a laser stripe similar to the one in [28] was employed to image RSAs of plants in a gel-based platform. As pointed out earlier, the proposed system is quite inexpensive while it provides a dense, precise and accurate 3D point cloud. However, as with any other active sensor for the same application, the use of SLS results in distorted models due to the refraction of the light through the various changes of media – air-to-glass, glass-to-gel, and back. These distortions are compensated by the system presented here.
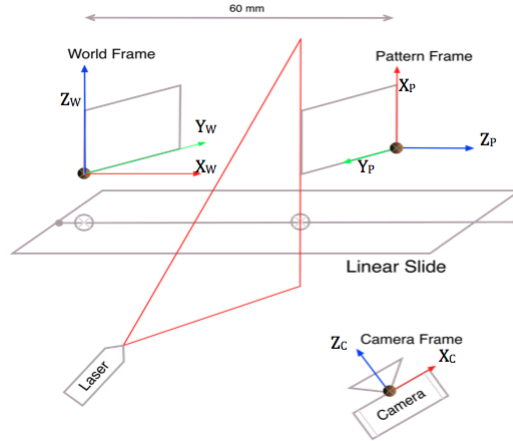
Fig. 3: Details on the SLS and its choices of coordinate frames. The figure shows the World, the Pattern, and the Camera coordinate frames with the actual orientations used in this paper: e.g., the XY plane of the pattern was arbitrarily set parallel to the world YZ plane.

### 3.1   Hardware Setup

The hardware used in our setup consists of three parts: 1) a laser light source (Lasiris Structured Laser Light, 635nm, 5mW); 2) a firewire camera (Firefly MV FFMV-03M2C); and 3) a linear slide platform with a turn table, both controlled by a TS-7250 embedded device. A sketch and an actual picture of the system is presented in Figure 2.

In this setup, the plane created by the laser source is made approximately perpendicular to the direction of movement of the turn-table platform on the linear slide. As shown in Figure 2b, the liner slide moves along the X-axis and the rotary stage rotates about the Z-axis. The camera is connected to a computer through a firewire port and it is calibrated for the extrinsic and intrinsic parameters by placing a chess board at the origin of the pattern coordinate frame – refer to Figure 3. The calibration of the intrinsic and extrinsic parameter of the camera as well as of its lens distortions are performed using the algorithm described in [28]. Because of this calibration, in the next sections, it will be assumed that the camera lenses produce undistorted 2D images of the scene. The world reference frame, indicated in Figure 3, is the coordinate frame with respect to which the position of the laser, the center of the camera and the position of the axis of the gel cylinder are calibrated.

### 3.2   Creating 3D Models

In this section, we explain in detail the data acquisition process employed by the SLS; the proposed technique for compensating for distortion due to light refraction; and the process to create the final 3D model.

**Data Acquisition:**   First, roots are grown inside the gel cylinder as shown in Figure 4. Then, the gel platform is placed on the linear slide which is moved back and forth for scanning the plant. One

(a)

Fig. 4: Image of a root growing inside a gel-based platform

complete scan consists of moving the linear slide forward in front of the laser and then backwards to its initial position, followed by a rotation of the turn table by a predefined angle around its vertical axis. This process is repeated until the root is observed from all 360 degrees.

The linear slide has four different phases: 1) Ramp-up, which is when the slide accelerates to reach the desired velocity; 2) Constant-speed, when the slide moves with a constant velocity; 3) Ramp-down, when the slide decelerates to a full stop; and 4) Quick return to origin and rotate the turn-table. As pointed out earlier, the world frame – shown in Figure 3 – is chosen in such a way that the position of the linear slide at the beginning of its constant-speed phase coincides with the origin of the world coordinate frame. Also, at that moment, images of the root are grabbed and stored in sequence, until the linear slide reaches the end of the constant-speed phase. The camera is synchronized with the embedded device that controls the liner slide.

Every image in a scan registers the shape of the laser stripe at a specific position of the linear slide, as illustrated in Figure 2a – i.e. the index $j$ of an image file saved by the system corresponds directly to a position of the linear slide in the X direction of the World coordinate frame. Also, the row value $v^j$ of a pixel on the laser stripe in the image plane $j$ relates to the height of the corresponding point on the object/root – as measured by the Z coordinate in the World frame. Similarly, the column value $u^j$ of that same pixel relates to the depth of the object in space – this time along the Y coordinate in the World frame. In summary, the relation between the image coordinate $(u^j,\ v^j)$ of a pixel on the laser stripe in the $j^{th}$ image and the corresponding space coordinate $(x^j,\ y^j,\ z^j)$ of the object being illuminated by the laser stripe is given by the following equations:

$$\begin{bmatrix} \bar{x}^j \\ \bar{y}^j \\ \bar{z}^j \\ \rho^j \end{bmatrix} = T * \begin{bmatrix} v^j \\ u^j \\ 1 \end{bmatrix}$$

$$\begin{bmatrix} x^j \\ y^j \\ z^j \end{bmatrix} = \begin{bmatrix} \bar{x}^j/\rho^j \\ \bar{y}^j/\rho^j \\ \bar{z}^j/\rho^j \end{bmatrix} + \begin{bmatrix} x_0 + (j-1)\Delta x \\ 0 \\ 0 \end{bmatrix}$$

(1)

where T is a $4x3$ transformation matrix calculated as described in [28], $\rho^j$ is a scale factor, $\Delta x$ is the step taken by the linear slide between each consecutive image acquisitions, and $x_0 = 0$.

If the camera and the root were immersed in the same medium (e.g. air), then these would be the final space coordinates of the illuminated pixel on the root. However, since the root is placed in a different medium, the $(u^j, v^j)$ values observed by the camera are actually distorted due to the refractive indexes of the different media – leading to the calculation of the wrong spacial coordinates from eq(1). The process to undistort these coordinates is explained in the next section.

**Undistorting the Cloud of Points:** As the laser stripe travels from the laser source, through the gel, off the root and onto the camera sensor, it refracts several times, each refraction depends on the angle of incidence with the specific medium change and their refractive indexes. In order to compensate for the consequent distortions, we must account for each one of the refractions in sequence. Also, to better explain this process, we will separate them into three parts: First, we will account for the refractions as the light coming from the illuminated root travels towards the camera; Then, the refractions as the laser penetrates the glass and gel until it hits the root; and Finally, we will combine these two paths of the light in order to determine the actual position of the desired point on the root.

However, before we can explain the three steps above, we must first calculate the position of the glass cylinder and the camera optical center. These will be required later on in order to calculate the cylinder surface normals and the refracted and incident rays.
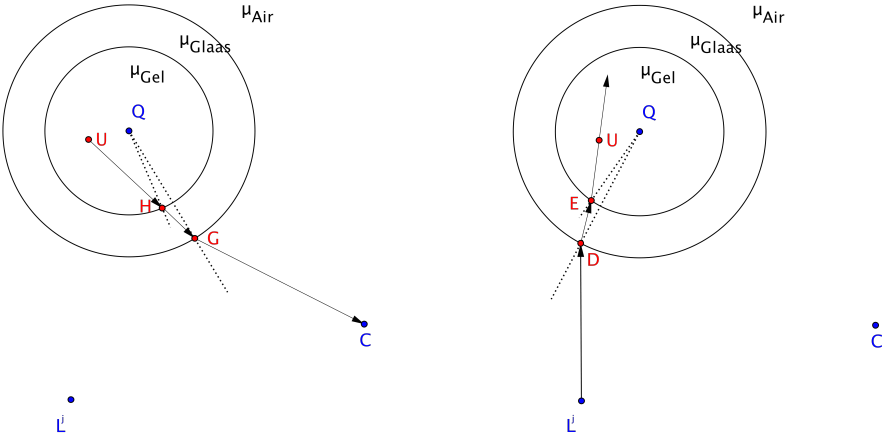


(a) Refraction of the laser coming of the scene. As the point G & H are not on the same plane, we will have center $Q_k$, where k=1,2.

(b) Refraction of the laser going into the scene. The point D and E are on the same plane, hence the center Q will be the same for these points.

Fig. 5: Refraction on the Cylinder due to Laser and Camera

***Calculating the Positions of Cylinder and Camera Center:*** In order to calculate the position of the vertical axis of the cylinder, we must emphasize that the image acquisition is synchronized with the motion of the linear slide. Hence, we can express the X coordinate of the center of the cylinder as a function of the index of the image $j$, the velocity of the slide in mm/sec $V_{slide}$, and the speed of the camera in frames/sec $S_{canera}$. In summary, the X-coordinate of the center of the cylinder is given by:

$$X^j = \Delta x * (j-1) = \frac{V_{slide}}{S_{camera}} * (j-1)$$

Additionally, since the cylinder moves only in the X direction, $Y^j = 0$ and $Z^j = z^j$, where $z^j$ is obtained from eq(1) for any given pixel $(u^j, v^j)$. So, the center of the cylinder is given by:

$$Q = \begin{bmatrix} X^j, 0, z^j \end{bmatrix} \tag{2}$$

Also, the center of the camera $C$ can be evaluated directly from the extrinsic parameters $^C H_P$ and the transformation matrix between the pattern and the world coordinate frames $^P H_W$, both obtained during camera calibration. That is, given:

$$^W H_C = \left( ^C H_P * {}^P H_W \right)^{-1}$$

the center of the camera frame is:

$$[X_c, Y_c, Z_c, 1]^T = {}^W H_C * [0, 0, 0, 1]^T \tag{3}$$

**Reversed Ray-tracing from Camera:** We are now ready to consider the actual refractions of the light through the glass/gel cylinder. As shown in Figure 5a, the light coming from the root inside the gel suffers two consecutive refractions before reaching the camera. These refractions are due to the thickness of the glass cylinder. So, in order to compensate for this component of the distortion, we follow a reversed ray tracing method similar to the one proposed in [39].

As also shown in the Figure 5a, we let $\overrightarrow{GC}$ be the direction of the ray converging to the image pixel $(u^j, v^j)$ and passing through the camera center $C$. This direction can be easily calculated from $(u^j, v^j)$ and $C$ alone using eq(3) – i.e. without actual knowledge of $G$ – the point at the intersection of $\overrightarrow{GC}$ and the external surface of the glass cylinder. Once this direction $\overrightarrow{GC}$ is found, and using the equation of a cylinder with X-Y coordinates of its center $Q_1$ given by eq(2) and diameter $d_{ext}$, finding the coordinate of $G$ becomes a trivial algebraic exercise. The missing Z coordinate of $Q_1$ is then the same as the Z coordinate of $G$.

This $G$ point on the surface of the cylinder is the point where the last refraction takes place: i.e. as the light finally leaves a denser medium (glass) into a rarer medium (air). Following Snell's Law of Refraction and its equation, we can calculate the incident ray at that point $G$. But first, we have to calculate the normal to the cylinder at $G$, which is defined as:

$$\overrightarrow{Q_1 G} = \frac{G - Q_1}{\|G - Q_1\|}$$

From the normal $\overrightarrow{Q_1 G}$ and the refracted ray $\overrightarrow{GC}$, and given that these are both unity vectors, the angle of refraction is calculated using their cross product:

$$sin(\theta_{air}) = \left\| \overrightarrow{Q_1G} \times \overrightarrow{GC} \right\| \tag{4}$$

We denote this angle $\theta_{air}$ because the refracted ray along $\overrightarrow{GC}$ travels indeed through the *air*. Similarly, the incidence angle will be denoted $\theta_{glass}$, and that angle can be found using Snell's equation: $\mu_{glass} * sin(\theta_{glass}) = \mu_{air} * sin(\theta_{air})$, where $\mu_{glass}$ and $\mu_{air}$ are the refractive indexes of the glass (incident) and air (refractive) media, respectively. And hence:

$$sin(\theta_{glass}) = \frac{\mu_{air} * sin(\theta_{air})}{\mu_{glass}}$$

From the system setup in Figure 2, one can infer that the direction $\overrightarrow{GC}$ is not necessarily horizontal (i.e. parallel to the world XY plane). So in order to calculate the actual incident ray, we will use the plane containing the incident ray, the refracted ray and the normal of the surface of the glass cylinder at the point $G$. This plane is known to exist also due to Snell's Law of Refraction and it is given by its surface normal, which can be determined by:

$$\overrightarrow{SN1_C} = \overrightarrow{Q_1G} \times \overrightarrow{GC} \tag{5}$$

Finally, the actual incident ray can be expressed using the vector $\overrightarrow{Q_1G}$ rotated about the vector $\overrightarrow{SN1_C}$ by an angle of $\theta_{glass}$ – which can be easily accomplished, for example, through an operation with unity quaternions [15]. This incident ray, $\overrightarrow{HG}$, is the direction of the ray emerging from the internal surface of the cylinder towards the camera, through the glass. This ray intersects the internal surface of the cylinder at point $H$, which again can be calculated using the direction $\overrightarrow{HG}$ and the equation of a cylinder with center $Q_2$ and diameter $d_{int}$. Once again, we must remember that the rays converging into the camera are not necessarily horizontal, thus the center $Q_2$ differs from $Q_1$, and it needs to be found. Luckily, $Q_2$ has the same Z coordinate as $H$ and hence, it can be expressed as $Q_2 = \begin{bmatrix} X^j, \ 0, \ H_z \end{bmatrix}^T$.

Next, we need to find the actual ray emerging from the root at point $U$ inside the gel (Figure 5a). Since the normal of the surface of the cylinder at $H$ can be expressed by:

$$\overrightarrow{Q_2H} = \frac{H - Q_2}{\|H - Q_2\|}$$

From here one, the process above for the outside surface of the cylinder can be repeated for its inside surface. In that way, we derive the refracted angle $\alpha_{glass}$ using eq(4) for $\overrightarrow{HG}$ and $\overrightarrow{Q_2H}$. Then, the angle of incidence $\alpha_{gel}$ at $H$ can be determined as a function of the refracted angle $\alpha_{glass}$ using Snell's equation and the refractive indexes $\mu_{glass}$ and $\mu_{gel}$. Next, the plane containing the incident ray $\overrightarrow{UH}$, the refracted ray $\overrightarrow{HG}$, and the normal $\overrightarrow{Q_2H}$ of the surface of the glass cylinder at the point $G$ can be represented by its surface normal $\overrightarrow{SN2_C}$ using an equation similar to eq(5). Finally, the emerging ray $\overrightarrow{UH}$ can be evaluated by rotating the vector $\overrightarrow{HG}$ by the angle $\alpha_{gel}$ about the vector $\overrightarrow{SN2_C}$.

**Ray-tracing from Laser:** Here, we start by assuming that the laser plane is vertical and so is the axis of the glass cylinder. It is also assumed that the laser is far from the cylinder in comparison to the typical heights of the roots to be scanned, and therefore the laser can be regarded as a diffused

line source with parallel rays. These two assumptions lead to the conclusion that the intensities of the refraction are the same for every point in the laser stripe – i.e. independent of the height at which the laser hits the cylinder. In terms of the coordinate frames presented in Figure 3, this means that distortions only occurs on the XY plane, and that the z-value of a point calculated with eq(1) is the same as the height of the illuminating laser ray.

Since the position of the laser is fixed w.r.t the world-frame, the point source of any laser ray can be expressed by $L^j : [x_l, y_l, z^j]^T$, where $x_l$ is the X-coordinate of the laser during calibration, $y_l$ is chosen arbitrarily large in the world Y-direction, and $z^j$ is obtained from eq(1) – refer to Figures 3 and 5b. It is important to mention also that $\overrightarrow{L^jD}$, representing the unity direction of the laser ray $L^j$, is always $[0,1,0]^T$ – once again, the laser plane is assumed vertical and the laser is positioned far from the scene in the Y opposite direction.

Similarly to what we did for the reversed ray-tracing approach from the camera, here the calculation of the refractions take the following (summarized) sequence: 1) use the direction $\overrightarrow{L^jD}$ to estimate the coordinate of $D$; 2) use $\overrightarrow{L^jD}$ and $\overrightarrow{QL^j}$ to determine $\gamma_{air}$; 3) use $\gamma_{air}$ and Snell's law to derive $\gamma_{glass}$; 4) use $\overrightarrow{L^jD}$ and $\overrightarrow{QL^j}$ to find the plane with surface normal $\overrightarrow{SN1_L}$; 5) rotate $\overrightarrow{L^jD}$ about $\overrightarrow{SN1_L}$ by $\gamma_{glass}$ to represent $\overrightarrow{DE}$; 6) use the direction $\overrightarrow{DE}$ to estimate the coordinate of $E$; 7) use $\overrightarrow{DE}$ and $\overrightarrow{QE}$ to determine $\phi_{glass}$; 8) use $\phi_{glass}$ and Snell's law to derive $\phi_{gell}$; 9) use $\overrightarrow{DE}$ and $\overrightarrow{QE}$ to find the plane with surface normal $\overrightarrow{SN2_L}$; and 10) rotate $\overrightarrow{DE}$ about $\overrightarrow{SN2_L}$ by $\phi_{gell}$ to represent $\overrightarrow{EU}$.

**Creating Undistorted Point Cloud:** Given $\overrightarrow{UH}$ and $\overrightarrow{EU}$ above, the undistorted point will be the point at intersection of these two vectors. Due to small errors in the calculation of $\overrightarrow{UH}$ and $\overrightarrow{EU}$, these two lines rarely intersect. For this reasons the intersection point is calculated as the midpoint on the line along the shortest distance between $\overrightarrow{UH}$ and $\overrightarrow{EU}$.

This whole process above is repeated for each of the points in the range image, creating the corresponding undistorted points in space.

**Final 3D Model:** After creating the point clouds for two consecutive scans, the clouds are registered into a single 3D point cloud using the Iterative Closest Points (ICP) algorithm [3]. The next scans are successively registered and appended to that same 3D point cloud to form the final 3D model of the root.

## 4   Experimental Results

For our experiments, we built a rectangular prism with square cross section. The prism, depicted in Figure 6, was inserted in a glass cylinder with internal and external radius of 41mm and 44mm, respectively. The dimension of the prism's cross section is $38mm \, x \, 38mm$. On the surface of the prism, three parallel white stripes were painted so that the coordinates of those stripes could be easily identified in the 3D models. The distance between the top and bottom stripes is 90mm. The refractive index of air, glass and water are assumed to be 1, 1.5 and 1.33 respectively. The proposed SLS scanned the prism from six different viewing angles, creating six point-clouds, with each consecutive view having been rotated by 60 degrees with respect to the previous one.

Because of the camera frame rate of 30 frames/sec and the desired resolution of the 3D model, the speed of the linear slide was set to 10mm/sec. As a result, in each scan 360 images were grabbed and then processed to create each of the six point clouds. At the end, all point clouds were registered and a single 3D model was created. The results for the distorted and undistorted point clouds are shown in Figure 7. It is important to mention here that the system takes 28 seconds to perform phase 1-3, as explained in section 3.2 and 17 seconds for phase 4. Hence, an entire scan using 6 views around the pattern took 270 seconds. For actual root phenotyping this time could be improved by using phase 4 also to scan the object in its return and/or by increasing the camera frame rate. However, a much more important consideration is that our setup was developed in our own lab using off-the-shelf and inexpensive mechanical components. A much faster system could be built to achieve much higher throughput.


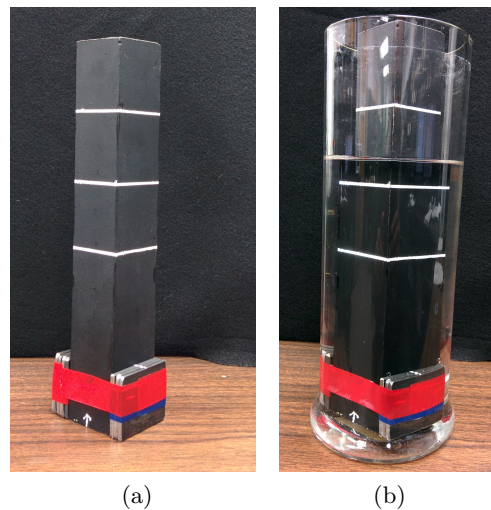
(a)                               (b)

Fig. 6: A rectangular prism with square cross section was used for calibration and testing of the proposed system. In a) is a view of the prism outside the cylinder; and in b) the same prism in a glass cylinder half filled with water illustrates the distortions observed by the 3D imaging system.

In order to check the accuracy of the proposed method, two sets of planes were estimated by fitting the points in the 3D clouds. Then, the relationship between those planes were compared against the actual measurements of the rectangular prism and the integrity of the reconstructed rectangular prism was inspected.

The first set of planes utilized the 3D points on each of the four vertical faces of the rectangular prism. The goal of this test was to check the integrity of the square cross section of the prism by computing the angle between these faces. Each face was numbered in sequence and Table 1 presents the dot product between the normals of each possible pair of planes. In Table 1a, we find the dot products related to the pairs of adjacent faces, while in Table 1b the dot product of the opposing faces. As expected, the adjacent faces are basically perpendicular to each other, while the opposing faces are parallel.
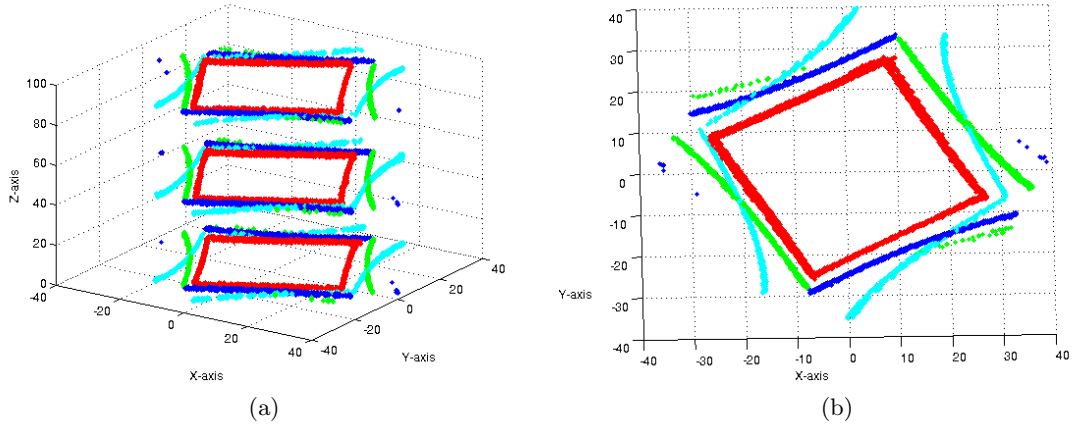
Fig. 7: 3D point cloud after registration of all six scans. The distorted points from scans 1 and 4 are plotted in dark blue; distorted points from scans 2 and 5 in green; and distorted scans 3 and 6 in cyan. The undistorted points from all six scans are plotted in red. In a) all point clouds for all three white stripes on the rectangular prims as depicted, while in b) only a single stripe is shown at closer look.

Next, to check the scale of the 3D cloud, the distances between points on opposing planes were measured. The mean and standard deviation of those distances for each pair of planes is shown in Table 2. Again, as the results indicate, the width of the prism was also preserved during reconstruction process.

| Used Planes | Measured Value |
| --- | --- |
| 1 & 2 | 0.0204 |
| 2 & 3 | 0.0128 |
| 3 & 4 | -0.0024 |
| 4 & 1 | 0.0052 |

(a)

| Used Planes | Measured Value |
| --- | --- |
| 1 & 3 | 0.9998 |
| 2 & 4 | 1.0000 |

(b)

Table 1: Relation between the four vertical faces of the reconstructed rectangular prism: a) dot product between the normal vectors of adjacent faces; and b) dot product of opposing faces.

Similarly, to check the noise level of the coordinates of the points on each plane, the distance between these points and their own planes was also calculated. Table 3a summarizes these results. Once again, the small mean and standard deviation obtained prove that the rectangular prism was reconstructed with a small error. Table 3b also presents a comparison between our method and the method in [39]. The mean and standard deviation of the error from both methods is summarized as a function of the distance from the laser.

| Used Planes | Mean (mm) | Std (mm) |
|:---:|:---:|:---:|
| 1 & 3 | 38.0217 | 0.2085 |
| 2 & 4 | 38.0017 | 0.3622 |
| 3 & 1 | 38.0227 | 0.2056 |
| 4 & 2 | 38.0022 | 0.4240 |

Table 2: Mean and standard deviation of the distances between the points on the first indicated plane and the second indicated plane (e.g. first row shows the distance of the points on plane 1 with respect to entire plane 3).

| Used Planes | Mean (mm) | Std (mm) |
|:---:|:---:|:---:|
| 1 | 0.1505 | 0.1095 |
| 2 | 0.1853 | 0.1452 |
| 3 | 0.1455 | 0.1265 |
| 4 | 0.1273 | 0.1053 |

(a)

| Laser Distance | Method in [39] | Our Method |
|:---:|:---:|:---:|
| | (mm) | |
| 239.24 | 0.31/0.14 | - |
| 500.37 | 0.73/0.55 | - |
| 300 | - | 0.1563/0.1243 |

(b)

Table 3: a)Mean and standard deviation of the distances from points on the indicated plane to that same plane. b) Comparison (mean/std) of the error from our method versus the method in [39] as a function of the distance from the laser.

Finally, a second set of planes was estimated, this time by fitting the points on the white stripes. In this case, the planes are horizontal and they slice the rectangular prism at three different heights.

Given both this second set of planes and the first set of planes (vertical faces), a set of dot products was again calculated. This time, the goal was to show the perpendicularity of the planes through the white stripes and the vertical faces of the prism. Table 4 presents the dot products between the top most plane and the bottom most plane with each of the face planes. Once again, a value close to zero indicates the almost perpendicularity between these planes.

| Face Plane | Top Plane | Bottom Plane |
|:---:|:---:|:---:|
| 1 | 0.0102 | 0.0112 |
| 2 | -0.0038 | -0.0069 |
| 3 | 0.0112 | 0.0122 |
| 4 | 0.0047 | 0.0015 |

Table 4: Dot Product between the planes on the top and bottom stripes and the vertical faces of the rectangular prism.

The distances between the points on the top most plane with respect to the bottom most plane were calculated and the result is summarized in the first row of Table 5. The reverse, i.e. the points on the bottom most plane with respect to the top plane is shown on the second row of that same table. As before, the goal here is to show the level of noise of the reconstructed 3D points and that such noise was not affected by the height of the laser rays (which were assumed parallel in Section

3.2:Ray-tracing from Laser). The results are once again very close to the ground truth – in this case, 90mm.

| Used Planes | Mean (mm) | Standard Deviation |
|---|---|---|
| Top plane and bottom plane | 89.9600 | 0.1457 |
| Bottom plane and top plane | 89.9600 | 0.0834 |

Table 5: Distance from opposing horizontal planes.

The next and final test involved real roots immersed in the gel inside the cylinder. This more qualitative test was performed for various roots and four examples were already presented at the beginning of this paper, in Figure 1, but due to page limitations the remaining tests will not be presented here. For this test, the refractive index of the gel was assumed to be 1.42. As Figure 1 shows, the quality of the 3D model from the undistorted method is quite superior when compared to the 3D model from the distorted points.

## 5    Conclusion and Future work

In this work, a new and complete method for undistorting 3D point clouds from a SLS was presented. The source of distortion is in the refraction of the light as it travels through the different media of the commonly used setup of glass/gel cylinder. These distortions have been neglected in many of the recent works in the literature. While in some cases the size of the root system in comparison to the glass/gel cylinder indeed minimizes the error, not all species of plants can benefit from this simplification. Besides, as the results presented here demonstrate, the quality of the 3D model can be very poor if the proposed method is not employed.

In the future, the thickness of the cylinder will be estimated as part of an optimization method to further improved the distortion model. Also, the various refractive indexes should also be estimated in order to further optimize the 3D reconstruction of the RSA. However, despite the already good results achieved here, the greatest improvement to be made is with respect to the assumption of parallel laser rays. In practice, it is not convenient to mount the laser far enough from the scene, not to mention the implications in the quality of the image due to its limited power. This fact certainly contributed for the errors obtained in the current work.

Other minor but certain improvements can be obtained by employing a higher resolution camera, a thinner laser stripe and cameras with faster frame rates.

## 6    Acknowledgement

# References

1. Agin, G., Binford, T.: Computer Description of Curved Objects. Computers, IEEE Transactions on C-25(4), 439–449 (1976)
2. Besl, P.J.: Advances in Machine Vision. chap. Active Optical Range Imaging Sensors, pp. 1–63. Springer-Verlag New York, Inc., New York, NY, USA (1988), http://dl.acm.org/citation.cfm?id=57360.57361
3. Besl, P., McKay, N.D.: A method for registration of 3-D shapes. Pattern Analysis and Machine Intelligence, IEEE Transactions on 14(2), 239–256 (1992)
4. Bidel, L.P.R., Pagès, L., Rivière, L.M., Pelloux, G., Lorendeau, J.Y.: Massflowdyn i: A carbon transport and partitioning model for root system architecture. Annals of Botany 85(6), 869–886 (2000), http://aob.oxfordjournals.org/content/85/6/869.abstract
5. Bowman, D., Devitt, D., Engelke, M., Rufty Jr., T.: Root architecture affects nitrate leaching from bentgrass turf. Crop Science 38(6), 1633–1639 (1998), http://www.scopus.com/inward/record.url?eid=2-s2.0-0032447708&partnerID=40&md5=aeea90ddd24b67be28c236f5d178d118, cited By (since 1996)48
6. Chen, C.H., Kak, A.: Modeling and calibration of a structured light scanner for 3-D robot vision. In: Robotics and Automation. Proceedings. 1987 IEEE International Conference on. vol. 4, pp. 807–815 (1987)
7. Chen Ying L., Dunbabin Vanessa M., Diggle Art J., Siddique Kadambot H. M., Rengel Zed: Development of a novel semi-hydroponic phenotyping system for studying root architecture. Functional Plant Biology 38(5), 355–363 (2011)
8. Clark, R.T., MacCurdy, R.B., Jung, J.K., Shaff, J.E., McCouch, S.R., Aneshansley, D.J., Kochian, L.V.: Three-Dimensional Root Phenotyping with a Novel Imaging and Software Platform. Plant Physiology 156(2), 455–465 (Jun 2011), http://dx.doi.org/10.1104/pp.110.169102
9. Doussan, C., Pagès, L., Vercambre, G.: Modelling of the hydraulic architecture of root systems: An integrated approach to water absorption - Model description. Annals of Botany 81, 213–223 (1998)
10. Fang, S., Yan, X., Liao, H.: 3D reconstruction and dynamic modeling of root architecture in situ and its application to crop phosphorus research. The Plant Journal 60(6), 1096–1108 (2009), http://dx.doi.org/10.1111/j.1365-313X.2009.04009.x
11. French, A., Ubeda-Tomás, S., Holman, T.J., Bennett, M.J., Pridmore, T.: High-Throughput Quantification of Root Growth Using a Novel Image-Analysis Tool. Plant Physiology 150(4), 1784–1795 (2009), http://www.plantphysiol.org/content/150/4/1784.abstract
12. Fua, P.: Reconstructing complex surfaces from multiple stereo views. In: Computer Vision, 1995. Proceedings., Fifth International Conference on. pp. 1078–1085 (1995)
13. Gregory, P., Hutchison, D., Read, D., Jenneson, P., Gilboy, W., Morton, E.: Non-invasive imaging of roots with high resolution X-ray micro-tomography. Plant and Soil 255(1), 351–359 (2003), http://dx.doi.org/10.1023/A:1026179919689
14. Heeraman, D., Hopmans, J., Clausnitzer, V.: Three dimensional imaging of plant roots in situ with X-ray Computed Tomography. Plant and Soil 189(2), 167–179 (1997), http://dx.doi.org/10.1023/B:PLSO.0000009694.64377.6f
15. Horn, B.K.P.: Closed-form solution of absolute orientation using unit quaternions. Journal of the Optical Society of America A 4(4), 629–642 (1987)
16. Idesawa, M., Yatagai, T., Soma, T.: Scanning moiré method and automatic measurement of 3-D shapes. Appl. Opt. 16(8), 2152–2162 (Aug 1977), http://ao.osa.org/abstract.cfm?URI=ao-16-8-2152
17. Iyer-Pascuzzi, A.S., Symonova, O., Mileyko, Y., Hao, Y., Belcher, H., Harer, J., Weitz, J.S., Benfey, P.N.: Imaging and Analysis Platform for Automatic Phenotyping and Trait Ranking of Plant Root Systems. Plant Physiology 152(3), 1148–1157 (2010), http://www.plantphysiol.org/content/152/3/1148.abstract
18. Jahnke, S., Menzel, M.I., Van Dusschoten, D., Roeb, G.W., Bühler, J., Minwuyelet, S., Blümler, P., Temperton, V.M., Hombach, T., Streun, M., Beer, S., Khodaverdi, M., Ziemons, K., Coenen, H.H., Schurr, U.: Combined MRI–PET dissects dynamic changes in plant structures and functions. The Plant Journal 59(4), 634–644 (2009), http://dx.doi.org/10.1111/j.1365-313X.2009.03888.x
19. Kak, A.C., Slaney, M.: Principles of Computerized Tomographic Imaging. IEEE Press, New York (1988)

20. Kazo, C., Hajder, L.: High-quality structured-light scanning of 3D objects using turntable. In: Cognitive Infocommunications (CogInfoCom), 2012 IEEE 3rd International Conference on. pp. 553–557 (2012)

21. Lam, D., Hong, R.Z., DeSouza, G.: 3D human modeling using virtual multi-view stereopsis and object-camera motion estimation. In: Intelligent Robots and Systems, 2009. IROS 2009. IEEE/RSJ International Conference on. pp. 4294–4299 (2009)

22. LAMBERS, H., SHANE, M.W., CRAMER, M.D., PEARSE, S.J., VENEKLAAS, E.J.: Root structure and functioning for efficient acquisition of phosphorus: Matching morphological and physiological traits. Annals of Botany 98(4), 693–713 (2006), http://aob.oxfordjournals.org/content/98/4/693.abstract

23. Lobet, G., Pagès, L., Draye, X.: A Novel Image-Analysis Toolbox Enabling Quantitative Analysis of Root System Architecture. Plant Physiology 157(1), 29–39 (2011), http://www.plantphysiol.org/content/157/1/29.abstract

24. Lynch, J.: Root Architecture and Plant Productivity. Plant Physiology 109(1), 7–13 (1995), http://www.plantphysiol.org/content/109/1/7.short

25. Martin, W.N., Aggarwal, J.: Volumetric Descriptions of Objects from Multiple Views. Pattern Analysis and Machine Intelligence, IEEE Transactions on PAMI-5(2), 150–158 (1983)

26. Nakini, T., DeSouza, G.N., Prince, S.J., Musket, T., Murphy, M.C., T, N.H.: 3d imaging and feature extraction for root phenotyping of soybean. In: PhenoDays Symposium on Imaging & Robotics for the 21st Century (Sept 2013), danforth Plant Science Center, St. Louis, MO

27. Niem, W.: Robust And Fast Modelling Of 3D Natural Objects From Multiple Views. In: SPIE Proceedings Image and Video Processing II. vol. Volume 2182 (1994), http://www.cse.psu.edu; cg597d/papers/SPIE94-WN.pdf

28. Park J., DeSouza, G.N.: Photo-realistic Modeling of Three Dimensional Objects Using Range and Reflectance Data in Innovations in Machine Intelligence and Robot Perception. Springer-Verlag (2005)

29. Pound, M.P., French, A.P., Atkinson, J., Wells, D.M., Bennett, M.J., Pridmore, T.P.: RootNav: Navigating images of complex root architectures. Plant Physiology (2013), http://www.plantphysiol.org/content/early/2013/06/12/pp.113.221531.abstract

30. Ribaut, J.M., Betran, J., Monneveux, P., Setter, T.: Drought Tolerance in Maize. In: Bennetzen, J., Hake, S. (eds.) Handbook of Maize: Its Biology, pp. 311–344. Springer New York

31. Scheenen, T., Vergeldt, F., Heemskerk, A., Van As, H.: Intact Plant Magnetic Resonance Imaging to Study Dynamics in Long-Distance Sap Flow and Flow-Conducting Surface Area. Plant Physiology 144(2), 1157–1165 (2007), http://www.plantphysiol.org/content/144/2/1157.abstract

32. Silverberg, J.L., Noar, R.D., Packer, M.S., Harrison, M.J., Henley, C.L., Cohen, I., Gerbode, S.J.: 3d imaging and mechanical modeling of helical buckling in medicago truncatula plant roots. Proceedings of the National Academy of Sciences (2012), http://www.pnas.org/content/early/2012/09/19/1209287109.abstract

33. Topp, C.N., Iyer-Pascuzzi, A.S., Anderson, J.T., Lee, C.R., Zurek, P.R., Symonova, O., Zheng, Y., Bucksch, A., Mileyko, Y., Galkovskyi, T., Moore, B.T., Harer, J., Edelsbrunner, H., Mitchell-Olds, T., Weitz, J.S., Benfey, P.N.: 3D phenotyping and quantitative trait locus mapping identify core regions of the rice genome controlling root architecture. Proceedings of the National Academy of Sciences 110(18), E1695–E1704 (2013), http://www.pnas.org/content/110/18/E1695.abstract

34. Trachsel, S., Kaeppler, S., Brown, K., Lynch, J.: Shovelomics: high throughput phenotyping of maize (Zea mays L.) root architecture in the field. Plant and Soil 341(1-2), 75–87 (2011), http://dx.doi.org/10.1007/s11104-010-0623-8

35. Tracy, S.R., Roberts, J.A., Black, C.R., McNeill, A., Davidson, R., Mooney, S.J.: The X-factor: visualizing undisturbed root architecture in soils using X-ray computed tomography. Journal of Experimental Botany 61(2), 311–313 (2010), http://jxb.oxfordjournals.org/content/61/2/311.short

36. Van As, H., Scheenen, T., Vergeldt, F.: MRI of intact plants. Photosynthesis Research 102(2-3), 213–222 (2009), http://dx.doi.org/10.1007/s11120-009-9486-3

37. van der Weerd, L., Claessens, M.M., Ruttink, T., Vergeldt, F.J., Schaafsma, T.J., Van As, H.: Quantitative NMR microscopy of osmotic stress responses in maize and pearl millet. Journal of Experimental Botany 52(365), 2333–2343 (2001), http://jxb.oxfordjournals.org/content/52/365/2333.abstract

38. Yamashita, A., Higuchi, H., Kaneko, T., Kawata, Y.: Three dimensional measurement of object's surface in water using the light stripe projection method. In: Robotics and Automation, 2004. Proceedings. ICRA '04. 2004 IEEE International Conference on. vol. 3, pp. 2736–2741 Vol.3 (April 2004)
39. Yamashita, A., Hayashimoto, E., Kaneko, T., Kawata, Y.: 3-D Measurement of Objects in a Cylindrical Glass Water Tank with a Laser Range Finder. In: Proceedings of the 2003 IEEE/RSJ International Conference on Intelligent Robots and Systems. pp. 1578–1583 (2003)
40. Yazdanbakhsh N., Fisahn J.: High throughput phenotyping of root growth dynamics, lateral root formation, root architecture and root hair development enabled by PlaRoM. Functional Plant Biology 36(11), 938–946 (2009)
41. Zha, H., Morooka, K., Hasegawa, T., Nagata, T.: Active modeling of 3-D objects: planning on the next best pose (NBP) for acquiring range images. In: 3-D Digital Imaging and Modeling, 1997. Proceedings., International Conference on Recent Advances in. pp. 68–75 (1997)
42. Zhu, T., Fang, S., Li, Z., Liu, Y., Liao, H., Yan, X.: Quantitative analysis of 3-dimensional root architecture based on image reconstruction and its application to research on phosphorus uptake in soybean. Chinese Science Bulletin 51(19), 2351–2361 (2006), http://dx.doi.org/10.1007/s11434-006-2130-0